Visualizing Staphylococcus aureus pathogenic membrane modification within the host infection environment by multimodal imaging mass spectrometry

Perry, William J.; Grunenwald, Caroline M.; Van de Plas, Raf; Witten, James C.; Martin, Daniel R.; Apte, Suneel S.; Cassat, James E.; Pettersson, Gösta B.; Caprioli, Richard M.; Skaar, Eric P.

DOI
10.1016/j.chembiol.2022.05.004

Publication date
2022

Document Version
Final published version

Published in
Cell Chemical Biology

Brief Communication

Cell Chemical Biology

Visualizing *Staphylococcus aureus* pathogenic membrane modification within the host infection environment by multimodal imaging mass spectrometry

Graphical abstract

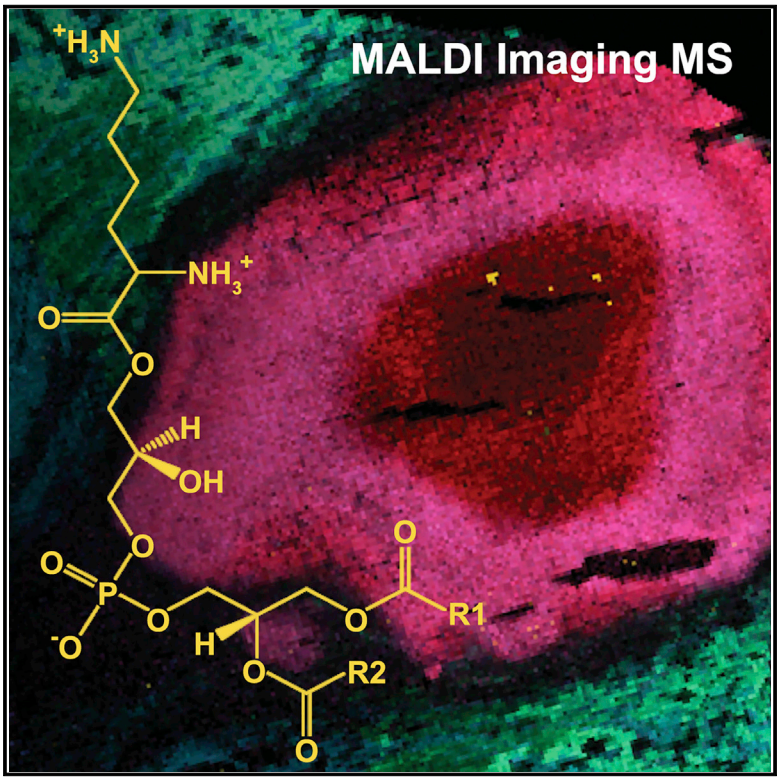

Highlights

- Multimodal imaging shows *S. aureus* envelope modification *in situ*
- Microscopy-IMS image fusion reveals *S. aureus* lysyl-PGs linked to bacterial foci
- Varied lipid profiles imply spatially driven *S. aureus* response to host defenses

Authors

William J. Perry, Caroline M. Grunenwald, Raf Van de Plas, ..., Richard M. Caprioli, Eric P. Skaar, Jeffrey M. Spraggins

Correspondence

eric.skaar@vumc.org (E.P.S.), jeff.spraggins@vanderbilt.edu (J.M.S.)

In brief

Perry et al. combine imaging mass spectrometry and microscopy to reveal *Staphylococcus aureus* envelope modifications within infected murine and human tissues. Their technique provides bacterial lipid profiles that highlight varied lysyl-phosphatidylglycerol distributions suggesting a heterogeneous, spatially oriented microbial response to host defenses *in situ*.

Perry et al., 2022, Cell Chemical Biology *29*, 1209–1217
July 21, 2022
https://doi.org/10.1016/j.chembiol.2022.05.004

CellPress

Cell Chemical Biology

CellPress

Brief Communication

Visualizing *Staphylococcus aureus* pathogenic membrane modification within the host infection environment by multimodal imaging mass spectrometry

William J. Perry,[1,2,3] Caroline M. Grunenwald,[3,4] Raf Van de Plas,[1,5,6] James C. Witten,[7] Daniel R. Martin,[8] Suneel S. Apte,[8] James E. Cassat,[3,4,9,10] Gösta B. Pettersson,[7] Richard M. Caprioli,[1,2,6,11,12] Eric P. Skaar,[3,4,*] and Jeffrey M. Spraggins[1,2,6,13,14,*]

[1]Mass Spectrometry Research Center, Vanderbilt University, Nashville, TN 37232, USA
[2]Department of Chemistry, Vanderbilt University, Nashville, TN 37212, USA
[3]Vanderbilt Institute for Infection, Immunology, and Inflammation, Vanderbilt University, Nashville, TN 37232, USA
[4]Department of Pathology, Microbiology, and Immunology, Vanderbilt University Medical Center, Nashville, TN 37212, USA
[5]Delft Center for Systems and Control, Delft University of Technology - TU Delft, Delft, the Netherlands
[6]Department of Biochemistry, Vanderbilt University, Nashville, TN 37212, USA
[7]Department of Thoracic and Cardiovascular Surgery, Cleveland Clinic Heart and Vascular Institute, Cleveland, OH 44195, USA
[8]Department of Biomedical Engineering, Cleveland Clinic Lerner Research Institute, Cleveland, OH 44195, USA
[9]Department of Pediatrics, Division of Pediatric Infectious Diseases, Vanderbilt University Medical Center, Nashville, TN 37232, USA
[10]Department of Biomedical Engineering, Vanderbilt University Medical Center, Nashville, TN 37232, USA
[11]Department of Pharmacology, Vanderbilt University, Nashville, TN 37212, USA
[12]Department of Medicine, Vanderbilt University, Nashville, TN 37212, USA
[13]Department of Cell & Developmental Biology, Vanderbilt University, Nashville, TN 37232, USA
[14]Lead contact
*Correspondence: eric.skaar@vumc.org (E.P.S.), jeff.spraggins@vanderbilt.edu (J.M.S.)
https://doi.org/10.1016/j.chembiol.2022.05.004

SUMMARY

Bacterial pathogens have evolved virulence factors to colonize, replicate, and disseminate within the vertebrate host. Although there is an expanding body of literature describing how bacterial pathogens regulate their virulence repertoire in response to environmental signals, it is challenging to directly visualize virulence response within the host tissue microenvironment. Multimodal imaging approaches enable visualization of host-pathogen molecular interactions. Here we demonstrate multimodal integration of high spatial resolution imaging mass spectrometry and microscopy to visualize *Staphylococcus aureus* envelope modifications within infected murine and human tissues. Data-driven image fusion of fluorescent bacterial reporters and matrix-assisted laser desorption/ionization Fourier transform ion cyclotron resonance imaging mass spectrometry uncovered *S. aureus* lysyl-phosphatidylglycerol lipids, localizing to select bacterial communities within infected tissue. Absence of lysyl-phosphatidylglycerols is associated with decreased pathogenicity during vertebrate colonization as these lipids provide protection against the innate immune system. The presence of distinct staphylococcal lysyl-phosphatidylglycerol distributions within murine and human infections suggests a heterogeneous, spatially oriented microbial response to host defenses.

INTRODUCTION

The increased incidence of antimicrobial resistance among bacterial pathogens has emphasized the need to discover critical pathogenic adaptations that can be targeted to develop alternative or adjunctive therapeutics (Beceiro et al., 2013). *Staphylococcus aureus* is an increasingly antibiotic-resistant human pathogen, capable of causing a variety of life-threatening illnesses that range from soft tissue infections to serious systemic infections (Casadevall and Pirofski, 2000). Antimicrobials used to combat bacterial infections commonly function by disrupting critical microbial processes such as protein synthesis, energy production, and envelope stability and biogenesis (Kohanski et al., 2010). Cationic compounds, such as daptomycin, are one class of antimicrobial compounds that target envelope stability and are frequently used to combat Gram-positive bacterial infections. Moreover, host-generated cationic antimicrobial peptides (CAMPs) also bind or insert into bacterial membranes to compromise structural integrity (Muthaiyan et al., 2008). In response to these compounds, bacterial pathogens can aminoacylate anionic phosphatidylglycerol (PG) membrane lipids, thereby reducing electrostatic interactions as a mechanism to evade cationic compounds (Slavetinsky et al., 2017). *S. aureus*, in particular, is known to modify PG membrane lipids with lysine

residues (lysyl-PG) through the action of multiple peptide resistance factor (MprF), providing resistance to cationic compounds (Peschel et al., 2001).

Inflammatory lesions or abscesses within soft tissue are hallmarks of *S. aureus* infection. Abscess morphology consists of staphylococcal abscess communities (SACs) segregated from normal host tissue by layers of necrotic and healthy polymorphonuclear neutrophil (PMN) innate immune cells (Cheng et al., 2011). Recruited PMNs phagocytose bacteria and release numerous antimicrobial effectors including reactive oxygen and nitrogen species, antimicrobial peptides, and digestive enzymes (Kobayashi et al., 2015). Staphylococcal dissemination within a vertebrate host relies on a diverse array of virulence factors (Cheng et al., 2009). Many of these virulence factors function in evasion or resistance against immune-mediated killing. One such example is the production of lysyl-PGs by MprF and the subsequent incorporation of these modified PGs into the staphylococcal envelope. Comprised of synthase and flippase domains, MprF facilitates the transfer of lysine from lysyl-transfer RNA to phosphatidylglycerol lipids to then be translocated to the outer membrane leaflet (Ernst et al., 2009). The decreased net negative charge of the altered membrane decreases electrostatic attraction from positively charged antimicrobials providing resistance against these compounds (Ernst and Peschel, 2019). Absence of lysyl-PG production results in increased staphylococcal killing by human PMNs and attenuated virulence in a murine model of systemic infection (Peschel et al., 2001). Genetic modifications to MprF resulting in increased activity of the synthase or flippase domains have been identified that result in increased lysyl-PG abundance. Elevated lysyl-PG production results in altered resistance and susceptibility to daptomycin (Ernst and Peschel, 2019; Baltz, 2009; Mishra and Bayer, 2013).

Emerging literature suggests that the staphylococcal abscess is a molecularly heterogenous environment and therefore SACs elaborate differential gene expression across distinct abscesses and even within a single abscess (Cassat et al., 2018; Perry et al., 2019). The abundance and distribution of lysyl-PGs produced by staphylococcal communities within infected tissue has never been determined. The spatial structure and unique interplay of host and bacterial factors that comprise abscesses make *in vivo* studies of this interface challenging, and most technologies do not allow for the selection or enrichment of bacteria-specific metabolic factors from the complex chemical matrix of tissue. Isolating and identifying unique or heterogeneous molecular distributions within these infections can provide insight into potential pathogenic adaptations or resistant *S. aureus* subpopulations that are more likely to promote chronicity of infection.

Traditional discovery approaches for molecular investigation of tissue samples (e.g., liquid chromatography-mass spectrometry) require solubilization, eliminating spatial information and diluting low abundance analytes of interest. Matrix-assisted laser desorption/ionization imaging mass spectrometry (MALDI IMS) has proven its utility as an *ex vivo* technology to study host-pathogen chemical interactions at sites of infection (Cassat et al., 2018; Perry et al., 2019; Moore et al., 2014; Caprioli et al., 1997; Blanc et al., 2018; Scott et al., 2017; Juttukonda et al., 2017; Kehl-Fie et al., 2013; Spraggins et al., 2015; Wakeman et al., 2016). The distribution and abundance of any mass-to-charge ratio (*m/z*) can be mapped across the measurement area as an ion image (Caprioli et al., 1997). Recent advancements in IMS instrumentation allows for unprecedented molecular specificity and spatial fidelity, in some instances approaching sub-cellular resolution (Spraggins et al., 2019; Niehaus et al., 2019; Prentice et al., 2019). Despite advances in imaging technologies, there is no universal technology or modality that can capture all molecular and morphological information in a single experiment. Thus, the incorporation of multiple co-registered and computationally fused imaging modalities can provide a deeper understanding of how molecular signatures are linked to specific tissue features (Patterson et al., 2018; Van de Plas et al., 2015). Application of various endogenous fluorescent markers, such as transgenic host fluorophores or bacterial fluorescent reporters, can drive IMS data mining strategies and interpretation (Jones et al., 2020). In this workflow, fluorescence microscopy data can be obtained prior to IMS without influencing the molecular signatures detected by mass spectrometry. Furthermore, both datasets can be acquired from a single tissue section, eliminating any issues with registration between serial sections. Herein, we demonstrate the capabilities of multimodal molecular imaging for interrogating SAC molecular architecture by leveraging high performance MALDI Fourier transform ion cyclotron resonance (FT-ICR) IMS computationally fused with fluorescence micrographs of bacterial reporters to investigate the presence and distributions of *S. aureus* lysyl-PG lipids within soft tissue infections.

RESULTS

S. aureus lysyl-PGs are differentially abundant within murine tissue abscesses

To investigate molecular species colocalizing with SACs, *S. aureus* infected tissues were analyzed using a multimodal approach integrating fluorescence microscopy, MALDI IMS of lipids, and hematoxylin and eosin (H&E) staining (Figure 1). In a systemic model of staphylococcal infection, mice were intravenously inoculated with *S. aureus* P_{mntA}*rfp*, where red fluorescent protein (RFP) expression is driven by the *mntA* promoter (P_{mntA}), a gene whose expression increases upon manganese starvation (Table 1; Perry et al., 2019). Seven days post infection (DPI), tissues were harvested, frozen on dry ice, and thinly sectioned for analyses. Visual comparison of the H&E stain and the fluorescence micrograph show co-localization of the RFP fluorophores to the SACs (Figures 1A and 1B). All SACs present within the abscess express the RFP reporter. Fluorescence microscopy of the RFP reporter is a chemically non-destructive approach to distinguish bacterial foci prior to IMS. MALDI IMS (Figures 1C, S1, and S2) of various murine and/or bacterial molecular species highlights the power of IMS to molecularly interrogate complex tissue environments without the use of tags or labels.

To isolate and explore relationships of ions that localize to bacterial foci, data-driven image fusion was employed (Van de Plas et al., 2015). This computational method of data analysis connects the spatial and informational content of two imaging modalities by constructing a mathematical cross-modality model using multivariate (partial least squares) linear regression (Van de Plas et al., 2015). Data-driven image fusion has previously been utilized for predictive applications such as spatial sharpening and out-of-sample predictions (Van de Plas et al., 2015; Neumann

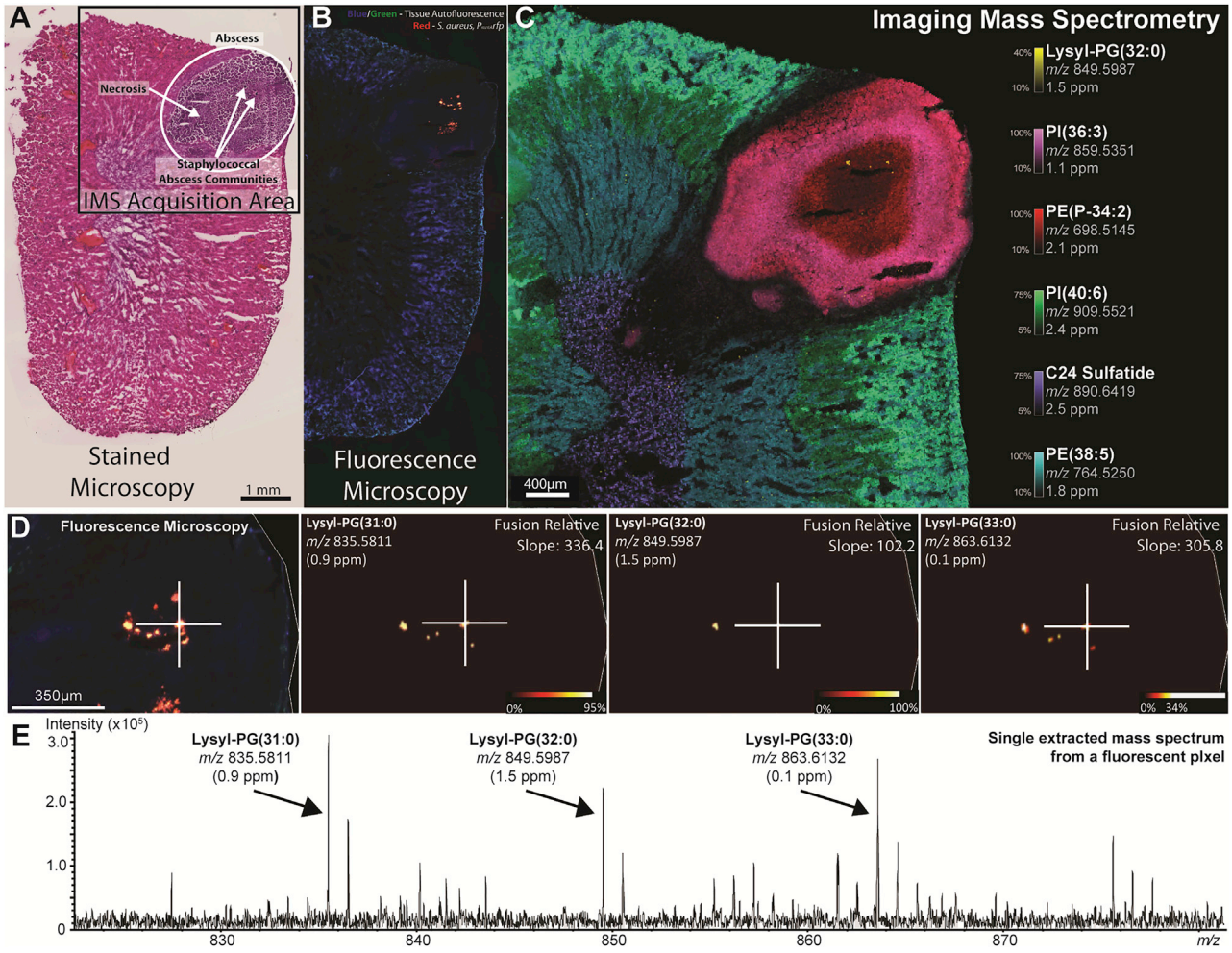

Figure 1. MALDI IMS spatially informed by fluorescence microscopy of *S. aureus*, P_{mntA}*rfp* maps chemical information from staphylococcal colonies

(A) H&E staining of a 7-DPI murine renal tissue section shows an abscess at the top right.

(B) A fluorescence micrograph of the same tissue section as (A) and (C) prior to MALDI IMS highlights the location of SACs (red fluorescent protein [RFP]).

(C) An ion overlay image highlights the various molecular constituents of the abscess and chemical complexity of the tissue section. These distributions also highlight kidney tissue substructures, such as the medulla and cortex.

(D) Lysyl-phosphatidylglycerol lipid species were isolated using image fusion data mining strategies (relative slopes shown) and identified by subsequent MALDI MS/MS experiments. The red crosshair is present to use as a reference point across the fluorescence micrograph zoom and ion images.

(E) A zoom of single extracted mass spectrum shows signals corresponding to lysyl-PG species.

See also Figures S1–S4.

et al., 2018; Lin et al., 2020). However, in this case, data-driven image fusion is used for a discovery-oriented application instead of a predictive one, utilizing only the first model-building phase of the fusion framework to mine relationships between the modalities, foregoing the second predictive phase that usually follows. The objective is to learn which relationships can be detected between the observations made in two distinct modalities. Since these relationships can be retrieved by opening up an empirically learned cross-modal model, the prediction portion of data-driven fusion is not necessary for this approach, and any uncertainties inherent to predictions are avoided. In this study, IMS images are tied to a fluorescence micrograph using fusion-learned multivariate linear models, isolating correlative relationships between the two modalities. Specifically, we searched for relationships between IMS data and the RFP bacterial reporter to isolate ions of bacterial origin.

Fusion of the IMS and fluorescence microscopy datasets revealed many ions with high correlations to the fluorescent reporters (Table 2). In this process, a fusion-generated, multivariate linear model that ties fluorescent reporters to IMS-reported ions is examined post-training phase, and the model's slope coefficients are used as heuristic measures for the strength of the relationship between a specific fluorescent reporter and a specific ion. If there is little to no relationship between the microscopy measurement and a variable (i.e., *m/z*) in the IMS data, then the slope that connects the two is relatively small or zero. If the slope is relatively large, a change in one microscopy variable correlates with significant change in the other IMS variable.

Table 1. *S. aureus* strains and plasmids used in this study

Strain	Genotype	Description	Reference
Newman	WT	Wild-type, methicillin-sensitive clinical isolate	(Duthie and Lorenz, 1952)
Newman	*mprF*::*erm*	In frame deletion of *mprF* gene marked with erythromycin resistance cassette	(Peschel et al., 2001)
Plasmid			
pOS1 P_{mntA} *rfp*		*mntA* promoter driving expression of a red fluorescent protein, responds to manganese starvation	(Cassat et al., 2018)

Table 2. Selected ions isolated by image fusion of IMS data and fluorescence microscopy of the RFP bacterial reporter

Ion rank	m/z	Lipid identification	Database matches	ppm Error	Image fusion relative slope
2	735.5178	PG(33:0)	3	0.6	544.1
7	797.6531	PE-Cer(d44:2)	1	1.4	354.2
8	616.4720	CerP(d34:1)	2	1.3	346.9
9	707.4871	PG(31:0)	3	0.3	343.9
10	835.5811	Lysyl-PG(31:0)	2*	0.9	336.4
12	863.6132	Lysyl-PG(33:0)	3*	0.1	305.8
15	747.5162	PG(34:1)	4	2.7	262.7
36	699.4974	PA(36:2)	4	0.5	174.7
44	721.5044	PG(32:0)	4	2.7	140.7
63	849.5987	Lysyl-PG(32:0)	1*	1.5	102.2

Lipid identifications are based on accurate measurements. Asterisks (*) indicate final identification using MS/MS data and was not present within the database. Part per million (ppm) errors are calculated using theoretical *m/z* values. Error values were calculated by comparison to a single extracted spectrum, calibrated internally using known lipid species. The image fusion relative slope is for the red channel, corresponding to the bacterial fluorescent reporter. Other ions and relative slopes for all fluorescence channels are in the supplemental information.

Database searching using The LIPID MAPS Lipidomics Gateway (http://www.lipidmaps.org/) resulted in tentative identification of many, but not all, ions of interest. MALDI MS/MS experiments to profile fluorescent bacterial foci resulted in the molecular identification of lysyl-PGs (Figure S3). Subsequent experiments using liquid chromatography coupled to MS/MS of *S. aureus* culture identified the presence of many PG and lysyl-PG lipids (Figure S3). Interestingly, lysyl-PGs in Figure 1D are not present at all locations of bacterial fluorophores. A more detailed comparison of heterogenous molecular profiles of SACs is presented in Figure S4. This suggests differential production of lysyl-PG across distinct SACs within the same abscess. An extracted MALDI MS spectrum (Figure 1E) from a single pixel colocalizing with an SAC is annotated for three lysyl-PGs. Notably, tissue abscesses were not observed when mice were infected with *S. aureus* Δ*mprF* (Figure S1). By employing multiple imaging modalities, heterogenous distributions of lysyl-PGs were mapped to staphylococcal communities within a murine infection model.

S. aureus lysyl-phosphatidylglycerols and host cationic antimicrobial peptides are present in human infective endocarditis tissue samples

Infective endocarditis is an infection of the endocardium, the inner tissue lining of cardiac chambers and valves. These infections are associated with both high morbidity and mortality among human patients and are characterized by bulky lesions that form on heart valves, called vegetations (Holland, Baddour, Bayer, Hoen, Miro, and Fowler, 2016). Like soft tissue abscesses, endocarditis vegetations are composed of recruited innate immune cells and SACs, as well as coagulation proteins and other blood components (Martin et al., 2020). *S. aureus* is the most common causative pathogen for this disease (Thuny et al., 2012; Cahill et al., 2017; Pettersson et al., 2014). As such, describing *S. aureus* human-specific virulence factors is critical for understanding the molecular architecture of infectious lesions (Onyango and Alreshidi, 2018; Dastgheyb and Otto, 2015). To investigate the presence of lysyl-PGs within these infections, infected valve tissue and vegetations from patients with community-acquired methicillin-sensitive *S. aureus* (CA-MSSA) infective endocarditis were subjected to MALDI IMS of lipids. Figure 2A shows a graphic of an infected aortic valve within a human heart. This highlights the location of the excised tissue shown in the H&E stain. The H&E stain is annotated for vegetation and valve regions. Ion images from MALDI IMS performed on a serial tissue section (Figure 2B) show localizations of both *S. aureus* PGs and lysyl-PGs. The selected ion images show that the distributions of the two lipids are not overlapping in this case.

Furthering this investigation of CA-MSSA endocarditis, MALDI IMS data of intact proteins were acquired from a serial tissue section. Spectral examination of the averaged IMS spectrum revealed the presence of two high intensity protein distributions at *m/z* 3371.47 and *m/z* 3442.54. Ion images of the two species revealed distributions that span the entirety of the vegetation regions (Figure 3A). Subsequent bottom-up LC-MS/MS workflows identified these analytes as α-defensin 2 and α-defensin 1 CAMPs, Figure 3B. Accurate mass measurements from FT-ICR IMS were used to link imaging data to LC-MS/MS identifications with low ppm mass errors. Notably, the CAMPs are absent from the valve tissue. It is hypothesized that the presence of CAMPs provokes lysyl-PG production as a stress response, potentially influencing the location of lysyl-PGs in the MALDI IMS of lipids from the serial tissue section (Roy, 2009). Expanding on the observations from a murine model of *S. aureus* infection, heterogeneous distributions of lysyl-PGs as well as host CAMPs were mapped to human infected tissue.

DISCUSSION

In this work, we mapped host and staphylococcal molecular responses within infection environments. A multimodal imaging approach combining fluorescence microscopy and MALDI IMS was mined using a computational strategy to isolate ions with correlative spatial relationships to a bacterial fluorescent reporter. A subsequent experiment identified many of the highly correlated ions to be lysyl-PG lipids. Lysyl-PGs and CAMPs

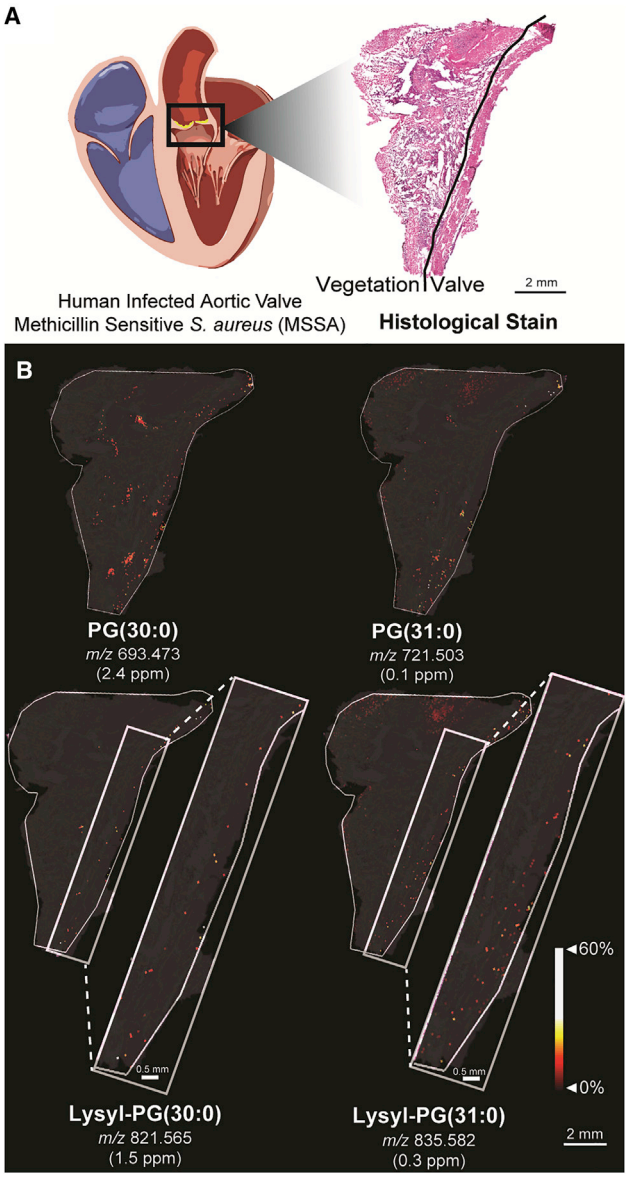

Figure 2. MALDI IMS of lipids from infective endocarditis tissue reveals *S. aureus* PGs and lysyl-PGs

(A) A graphic depicts infected human heart tissue lesions. A tissue stain of an infected heart lesion is annotated for normal and diseased tissue.

(B) Ion images of *S. aureus* PGs show distributions across the diseased tissue. Increased presence of lysyl-PGs can be observed near valve tissue (zoom).

were subsequently mapped to endocarditis infection within human tissue. Heterogeneous distributions of lysyl-PGs were observed from both experiments, highlighting the potential for niche-specific responses during infection.

These results provide insight into mechanisms of host innate immunity and bacterial pathogenesis at the site of infection. While the production of lysyl-PGs by *S. aureus* is attributed to virulence and antimicrobial resistance, this evasive response had yet to be observed *in vivo* (Ernst and Peschel, 2019; Baltz, 2009; Mishra and Bayer, 2013). Lysyl-PGs are not present at all SACs within a murine infection model. This suggests differential molecular responses to host stresses or mechanisms of innate immunity. Lysyl-PG distributions from a human endocarditis tissue sample show the heterogeneous presence of lysyl-PGs with *S. aureus* PGs and suggest variation in molecular responses, potentially relating to fitness. Distributions of α-defensin 1 and α-defensin 2 CAMPs localize to vegetations and are absent from valve tissue. However, increased presence of lysyl-PGs localizes near the valve tissue. Presence of the lipids at that location as well as the lack of CAMPs could be due to bacterial evasion of the innate immune system. Defensins were not observed in murine systemic infection models due to the lack of production by mice.

Many studies have highlighted the molecular heterogeneity present in *S. aureus* tissue infections (Cassat et al., 2018; Perry et al., 2019; Yao et al., 2010). While the *in vitro* roles of lysyl-PGs and other various pathogenic adaptations are known, it is not clear when and where these adaptations are most important during infection (Peschel et al., 2001; Ernst et al., 2009; Baltz, 2009; Mishra, and Bayer, 2013; Staubitz et al., 2004). Molecular heterogeneity across infectious foci could be explained by differential responses or mechanisms of host-pathogen interactions, highlighting the potential for niche-specific *S. aureus* pathogenic strategies. Organ-specific responses to infection may also exist. Increased understanding of when and where these pathogenic adaptations are required for bacterial proliferation can drive the search for alternative, novel therapeutics.

Spatially targeted and molecularly specific technologies such as MALDI IMS will assist in relating molecular heterogeneity to conditions, environments, or other previously uncharacterized molecular distributions to further elucidate host-pathogen interactions. Due to the lack of tags or labels, IMS allows for untargeted chemical information from a tissue surface, not achievable by other technologies. Furthermore, untargeted molecular analysis of staphylococcal infections, as provided by MALDI IMS, can drive the search for uniformly expressed bacterial factors, as these factors can serve as candidate vaccine targets. Incorporation of other imaging modalities to MALDI IMS, as exhibited here, allows for increased information about a tissue surface, expanding testable hypotheses. Application of automated data mining strategies, such as data-driven image fusion, can help isolate relationships between datasets. Leveraging this spatial information, chemical mechanisms of bacterial pathogenicity and antibiotic resistance as well as host innate immunity were mapped across infections in murine and human tissue.

Limitations of the study

We predict that the detection of heterogenous levels of bacterial lipids within the abscess is due to heterogenous abundance of these lipids throughout the staphylococcal microcolony. However, we are not able to quantify the specific number of bacteria within each microcolony, so it is possible that differences in the observed lipid levels are partially driven by differences in bacterial abundance throughout the lesion. We think this is unlikely since, qualitatively, there does not appear to be any correlation between lipid signals and bacterial abundance in a microcolony as determined by fluorescence. A second limitation involves the small number of samples imaged in these experiments. Obtaining infected human tissue is particularly challenging. Future work should expand these studies to include

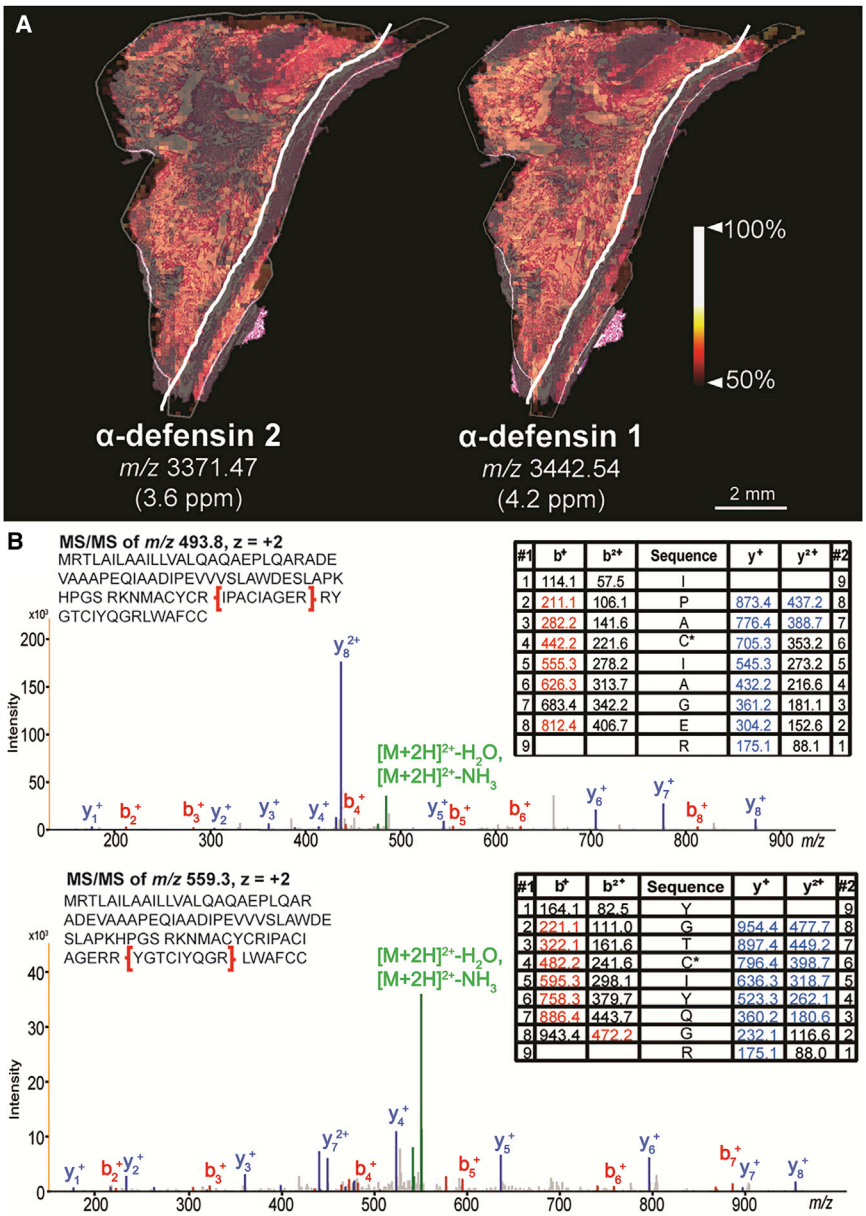

#1	b+	b2+	Sequence	y+	y2+	#2
1	114.1	57.5	I			9
2	211.1	106.1	P	873.4	437.2	8
3	282.2	141.6	A	776.4	388.7	7
4	442.2	221.6	C*	705.3	353.2	6
5	555.3	278.2	I	545.3	273.2	5
6	626.3	313.7	A	432.2	216.6	4
7	683.4	342.2	G	361.2	181.1	3
8	812.4	406.7	E	304.2	152.6	2
9			R	175.1	88.1	1

#1	b+	b2+	Sequence	y+	y2+	#2
1	164.1	82.5	Y			9
2	221.1	111.0	G	954.4	477.7	8
3	322.1	161.6	T	897.4	449.2	7
4	482.2	241.6	C*	796.4	398.7	6
5	595.3	298.1	I	636.3	318.7	5
6	758.3	379.7	Y	523.3	262.1	4
7	886.4	443.7	Q	360.2	180.6	3
8	943.4	472.2	G	232.1	116.6	2
9			R	175.1	88.0	1

Figure 3. MALDI IMS of intact proteins from an infective endocarditis vegetation reveals CAMPs colocalizing with diseased tissue

(A) Ion images of host CAMPs α-defensin 2 and α-defensin 1 show high abundances within vegetations.

(B) LC-MS/MS spectra from bottom-up proteomics workflows show peptides from α-defensin 2 and α-defensin 1.

larger numbers of samples, and distinct types of lesions, to determine the generalizability of these findings. Finally, like all analytical technologies, there are limitations to the capabilities of the MALDI imaging experiments performed here. There are likely multiple isomers for some of the bacterial lipid species detected due to the variety of potential acyl chain compositions that are possible. We do not think this detracts from the observed molecular heterogeneity because this would only mask potential variability. Improved specificity would further enhance our ability to detect molecular differences between bacterial colonies.

SIGNIFICANCE

Bacterial pathogens have evolved virulence factors to colonize, replicate, and disseminate within the vertebrate host. Although there is an expanding body of literature describing how bacterial pathogens regulate virulence repertoire in response to environmental signals, it is challenging to directly visualize virulence response within the host tissue microenvironment. Multimodal integration of high spatial resolution IMS and microscopy allow visualization of modifications to the *Staphylococcus aureus* envelope within infected murine and human tissues. Data mining strategies leveraging multimodal data-driven image fusion of fluorescent bacterial reporters and MALDI FT-ICR IMS revealed *S. aureus* lysyl-phosphatidylglycerol lipids localized to distinct bacterial communities within infected tissue. Varied staphylococcal lysyl-phosphatidylglycerol lipid distributions within murine and human infections suggests a heterogeneous, spatially oriented microbial response to host defenses.

STAR★METHODS

Detailed methods are provided in the online version of this paper and include the following:

- KEY RESOURCES TABLE
- RESOURCE AVAILABILITY
  - Lead contact
  - Materials availability
  - Data code and availability
- EXPERIMENTAL MODEL AND SUBJECT DETAILS
  - Bacterial strains and growth conditions
  - Murine model of systemic *S. aureus* infection
  - Infective endocarditis vegetations
- METHOD DETAILS
  - Materials
  - Sample preparation
  - Fluorescence microscopy image acquisition
  - Molecular image acquisition
  - Protein extraction for LC-MS/MS
  - LC-MS/MS proteomics data acquisition and analysis
  - LC-MS/MS of lipids from *S. aureus* culture
- QUANTIFICATION AND STATISTICAL ANALYSIS
  - Data-driven image fusion

SUPPLEMENTAL INFORMATION

Supplemental information can be found online at https://doi.org/10.1016/j.chembiol.2022.05.004.

ACKNOWLEDGMENTS

The authors thank Dr. Andreas Peschel (University of Tübingen, Germany) for contribution of the *S. aureus* strain inactivated for lysyl-PG production, *S. aureus* Δ*mprF*, and the Skaar Laboratory and MSRC for critical review of this manuscript. This work was funded by the NIH/National Institute of General Medical Sciences (2P41 GM103391-07 awarded to R.M.C.), the NIH National Institute of Allergy and Infectious Diseases (R01AI138581 awarded to E.P.S and J.M.S.; R01AI145992 awarded to E.P.S, J.M.S, and J.E.C.; R01AI132560 awarded to J.E.C; and R01AI069233, R01AI073843, and R01AI150701 awarded to E.P.S.), and the Burroughs Wellcome Fund. J.E.C. is also supported by a Career Award for Medical Scientists from the Burroughs Wellcome Fund. S.S.A. and D.R.M. are supported by the Allen Distinguished Investigator Program, through support made by The Paul G. Allen Frontiers Group and the American Heart Association (to S.S.A). The 15T FT-ICR MS in the Mass Spectrometry Research Center at Vanderbilt University was acquired through the NIH Shared Instrumentation Grant Program (1S10OD012359). The Fusion Lumos instrument at the Lerner Research Institute Proteomics and Metabolomics Core was purchased via an NIH shared instrument grant, 1S10OD023436-0.

AUTHOR CONTRIBUTIONS

W.J.P., J.M.S., R.M.C., and E.P.S. designed experiments. C.M.G. and J.E.C. performed animal infection models. W.J.P. completed bright-field microscopy, fluorescence microscopy, and LC-MS/MS lipidomics experiments. W.J.P. and J.M.S. completed MALDI IMS experiments. R.V.P. performed and analyzed the data-driven image fusion results. J.C.W. and G.B.P. provided the human tissue. D.R.M. and S.S.A. contributed LC-MS/MS proteomics data. W.J.P., J.M.S., and E.P.S. completed the original manuscript draft. All authors contributed to critical review and editing of the manuscript.

DECLARATION OF INTERESTS

The authors declare no interests.

Received: August 16, 2021
Revised: December 10, 2021
Accepted: May 11, 2022
Published: June 1, 2022

REFERENCES

Angel, P.M., Spraggins, J.M., Baldwin, H.S., and Caprioli, R. (2012). Enhanced sensitivity for high spatial resolution lipid analysis by negative ion mode matrix assisted laser desorption ionization imaging mass spectrometry. Anal. Chem. *84*, 1557–1564. https://doi.org/10.1021/ac202383m.

Baltz, R.H. (2009). Daptomycin: mechanisms of action and resistance, and biosynthetic engineering. Curr. Opin. Chem. Biol. *13*, 144–151. https://doi.org/10.1016/j.cbpa.2009.02.031.

Beceiro, A., Tomás, M., and Bou, G. (2013). Antimicrobial resistance and virulence: a successful or deleterious association in the bacterial world? Clin. Microbiol. Rev. *26*, 185–230. https://doi.org/10.1128/cmr.00059-12.

Blanc, L., Lenaerts, A., Dartois, V., and Prideaux, B. (2018). Visualization of mycobacterial biomarkers and tuberculosis drugs in infected tissue by MALDI-MS imaging. Anal. Chem. *90*, 6275–6282. https://doi.org/10.1021/acs.analchem.8b00985.

Bligh, E.G., and Dyer, W.J. (1959). A rapid method of total lipid extraction and purification. Can. J. Biochem. Physiol. *37*, 911–917. https://doi.org/10.1139/o59-099.

Cahill, T.J., Baddour, L.M., Habib, G., Hoen, B., Salaun, E., Pettersson, G.B., Schäfers, H.J., and Prendergast, B.D. (2017). Challenges in infective endocarditis. J. Am. Coll. Cardiol. *69*, 325–344. https://doi.org/10.1016/j.jacc.2016.10.066.

Caprioli, R.M., Farmer, T.B., and Gile, J. (1997). Molecular imaging of biological samples: localization of peptides and proteins using MALDI-TOF MS. Anal. Chem. *69*, 4751–4760. https://doi.org/10.1021/ac970888i.

Casadevall, A., and Pirofski, L.-a. (2000). Host-pathogen interactions: basic concepts of microbial commensalism, colonization, infection, and disease. Infect. Immun. *68*, 6511–6518. https://doi.org/10.1128/iai.68.12.6511-6518.2000.

Cassat, J.E., Moore, J.L., Wilson, K.J., Stark, Z., Prentice, B.M., Van de Plas, R., Perry, W.J., Zhang, Y., Virostko, J., Colvin, D.C., et al. (2018). Integrated molecular imaging reveals tissue heterogeneity driving host-pathogen interactions. Sci. Transl. Med. *10*. https://doi.org/10.1126/scitranslmed.aan6361.

Cheng, A.G., DeDent, A.C., Schneewind, O., and Missiakas, D. (2011). A play in four acts: *Staphylococcus aureus* abscess formation. Trends Microbiol. *19*, 225–232. https://doi.org/10.1016/j.tim.2011.01.007.

Cheng, A.G., Kim, H.K., Burts, M.L., Krausz, T., Schneewind, O., and Missiakas, D.M. (2009). Genetic requirements for *Staphylococcus aureus* abscess formation and persistence in host tissues. FASEB J *23*, 3393–3404. https://doi.org/10.1096/fj.09-135467.

Corbin, B.D., Seeley, E.H., Raab, A., Feldmann, J., Miller, M.R., Torres, V.J., Anderson, K.L., Dattilo, B.M., Dunman, P.M., Gerads, R., et al. (2008). Metal chelation and inhibition of bacterial growth in tissue abscesses. Science *319*, 962–965. https://doi.org/10.1126/science.1152449.

Dastgheyb, S.S., and Otto, M. (2015). Staphylococcal adaptation to diverse physiologic niches: an overview of transcriptomic and phenotypic changes in different biological environments. Future Microbiol. *10*, 1981–1995. https://doi.org/10.2217/fmb.15.116.

Duthie, E.S., and Lorenz, L.L. (1952). Staphylococcal coagulase: mode of action and antigenicity. Microbiology *6*, 95–107. https://doi.org/10.1099/00221287-6-1-2-95.

Ernst, C.M., Staubitz, P., Mishra, N.N., Yang, S.-J., Hornig, G., Kalbacher, H., Bayer, A.S., Kraus, D., and Peschel, A. (2009). The bacterial defensin resistance protein MprF consists of separable domains for lipid lysinylation and

antimicrobial peptide repulsion. PLoS Pathog. *5*, e1000660. https://doi.org/10.1371/journal.ppat.1000660.

Ernst, C.M., and Peschel, A. (2019). MprF-mediated daptomycin resistance. Int. J. Med. Microbiol. *309*, 359–363. https://doi.org/10.1016/j.ijmm.2019.05.010.

Holland, T.L., Baddour, L.M., Bayer, A.S., Hoen, B., Miro, J.M., and Fowler, V.G., Jr. (2016). Infective endocarditis. Nat. Rev. Dis. Primers. *2*, 16059. https://doi.org/10.1038/nrdp.2016.59.

Jones, M.A., Cho, S.H., Patterson, N.H., Van de Plas, R., Spraggins, J.M., Boothby, M.R., and Caprioli, R.M. (2020). Discovering new lipidomic features using cell type specific fluorophore expression to provide spatial and biological specificity in a multimodal workflow with MALDI Imaging Mass Spectrometry. Anal. Chem. *92*, 7079–7086. https://doi.org/10.1021/acs.analchem.0c00446.

Juttukonda, L.J., Berends, E.T.M., Zackular, J.P., Moore, J.L., Stier, M.T., Zhang, Y., Schmitz, J.E., Beavers, W.N., Wijers, C.D., Gilston, B.A., et al. (2017). Dietary manganese promotes staphylococcal infection of the heart. Cell Host Microbe *22*, 531–542.e8. https://doi.org/10.1016/j.chom.2017.08.009.

Kehl-Fie, T.E., Zhang, Y., Moore, J.L., Farrand, A.J., Hood, M.I., Rathi, S., Chazin, W.J., Caprioli, R.M., and Skaar, E.P. (2013). MntABC and MntH contribute to systemic *Staphylococcus aureus* infection by competing with calprotectin for nutrient manganese. Infect. Immun. *81*, 3395–3405. https://doi.org/10.1128/iai.00420-13.

Kobayashi, S.D., Malachowa, N., and DeLeo, F.R. (2015). Pathogenesis of *Staphylococcus aureus* abscesses. Am. J. Path. *185*, 1518–1527. https://doi.org/10.1016/j.ajpath.2014.11.030.

Kohanski, M.A., Dwyer, D.J., and Collins, J.J. (2010). How antibiotics kill bacteria: from targets to networks. Nat. Rev. Microbiol. *8*, 423–435. https://doi.org/10.1038/nrmicro2333.

Laut, C.L., Perry, W.J., Metzger, A.L., Weiss, A., Stauff, D.L., Walker, S., Caprioli, R.M., and Skaar, E.P. (2020). *Bacillus anthracis* responds to targocil-induced envelope damage through EdsRS activation of cardiolipin synthesis. mBio *11*. e03375–19. https://doi.org/10.1128/mbio.03375-19.

Lin, L.-E., Chen, C.-L., Huang, Y.-C., Chung, H.-H., Lin, C.-W., Chen, K.-C., Peng, Y.-J., Ding, S.-T., Wang, M.-Y., Shen, T.-L., and Hsu, C.-C. (2020). Precision biomarker discovery powered by microscopy image fusion-assisted high spatial resolution ambient ionization mass spectrometry imaging. Anal. Chim. Acta *1100*, 75–87. https://doi.org/10.1016/j.aca.2019.11.014.

Martin, D.R., Witten, J.C., Tan, C.D., Rodriguez, E.R., Blackstone, E.H., Pettersson, G.B., Seifert, D.E., Willard, B.B., and Apte, S.S. (2020). Proteomics identifies a convergent innate response to infective endocarditis and extensive proteolysis in vegetation components. JCI Insight *5*. https://doi.org/10.1172/jci.insight.135317.

Mishra, N.N., and Bayer, A.S. (2013). Correlation of cell membrane lipid profiles with daptomycin resistance in methicillin-resistant *Staphylococcus aureus*. Antimicrob. Agents Chemother. *57*, 1082–1085. https://doi.org/10.1128/aac.02182-12.

Moore, J.L., Caprioli, R.M., and Skaar, E.P. (2014). Advanced mass spectrometry technologies for the study of microbial pathogenesis. Curr. Opin. Microbiol. *19*, 45–51. https://doi.org/10.1016/j.mib.2014.05.023.

Muthaiyan, A., Silverman, J.A., Jayaswal, R.K., and Wilkinson, B.J. (2008). Transcriptional profiling reveals that daptomycin induces the *Staphylococcus aureus* cell wall stress stimulon and genes responsive to membrane depolarization. Antimicrob. Agents Chemother. *52*, 980–990. https://doi.org/10.1128/aac.01121-07.

Neumann, E.K., Comi, T.J., Spegazzini, N., Mitchell, J.W., Rubakhin, S.S., Gillette, M.U., Bhargava, R., and Sweedler, J.V. (2018). Multimodal chemical analysis of the brain by high mass resolution mass spectrometry and infrared spectroscopic imaging. Anal. Chem. *90*, 11572–11580. https://doi.org/10.1021/acs.analchem.8b02913.

Niehaus, M., Soltwisch, J., Belov, M.E., and Dreisewerd, K. (2019). Transmission-mode MALDI-2 mass spectrometry imaging of cells and tissues at subcellular resolution. Nat. Methods *16*, 925–931. https://doi.org/10.1038/s41592-019-0536-2.

Onyango, L.A., and Alreshidi, M.M. (2018). Adaptive metabolism in staphylococci: survival and persistence in environmental and clinical settings. J. Pathog. *2018*, 1–11. https://doi.org/10.1155/2018/1092632.

Patterson, N.H., Tuck, M., Van de Plas, R., and Caprioli, R.M. (2018). Advanced registration and analysis of MALDI imaging mass spectrometry measurements through autofluorescence microscopy. Anal. Chem. *90*, 12395–12403. https://doi.org/10.1021/acs.analchem.8b02884.

Perry, W.J., Spraggins, J.M., Sheldon, J.R., Grunenwald, C.M., Heinrichs, D.E., Cassat, J.E., Skaar, E.P., and Caprioli, R.M. (2019). *Staphylococcus aureus* exhibits heterogeneous siderophore production within the vertebrate host. Proc. Natl. Acad. Sci. U S A *116*, 21980–21982. https://doi.org/10.1073/pnas.1913991116.

Peschel, A., Jack, R.W., Otto, M., Collins, L.V., Staubitz, P., Nicholson, G., Kalbacher, H., Nieuwenhuizen, W.F., Jung, G., Tarkowski, A., et al. (2001). *Staphylococcus aureus* resistance to human defensins and evasion of neutrophil killing via the novel virulence factor mprf is based on modification of membrane lipids with lysine. J. Exp. Med. *193*, 1067–1076. https://doi.org/10.1084/jem.193.9.1067.

Pettersson, G.B., Hussain, S.T., Shrestha, N.K., Gordon, S., Fraser, T.G., Ibrahim, K.S., and Blackstone, E.H. (2014). Infective endocarditis: an atlas of disease progression for describing, staging, coding, and understanding the pathology. J. Thorac. Cardiovasc. Surg. *147*, 1142–1149.e2. https://doi.org/10.1016/j.jtcvs.2013.11.031.

Prentice, B.M., Ryan, D.J., Van de Plas, R., Caprioli, R.M., and Spraggins, J.M. (2019). Enhanced ion transmission efficiency up to m/z 24 000 for MALDI protein imaging mass spectrometry. Anal. Chem. *90*, 5090–5099. https://doi.org/10.1021/acs.analchem.7b05105.

Roy, H. (2009). Tuning the properties of the bacterial membrane with aminoacylated phosphatidylglycerol. IUBMB Life *61*, 940–953. https://doi.org/10.1002/iub.240.

Scott, A.J., Post, J.M., Lerner, R., Ellis, S.R., Lieberman, J., Shirey, K.A., Heeren, R.M.A., Bindila, L., and Ernst, R.K. (2017). Host-based lipid inflammation drives pathogenesis in *Francisella* infection. Proc. Natl. Acad. Sci. U S A *114*, 12596–12601. https://doi.org/10.1073/pnas.1712887114.

Slavetinsky, C., Kuhn, S., and Peschel, A. (2017). Bacterial aminoacyl phospholipids – biosynthesis and role in basic cellular processes and pathogenicity. Biochim. Biophys. Acta Mol. Cell Biol. Lipids *1862*, 1310–1318. https://doi.org/10.1016/j.bbalip.2016.11.013.

Spraggins, J.M., Djambazova, K.V., Rivera, E.S., Migas, L.G., Neumann, E.K., Fuetterer, A., Suetering, J., Goedecke, N., Ly, A., Van de Plas, R., and Caprioli, R.M. (2019). High performance molecular imaging with MALDI trapped ion mobility time-of-flight (timsTOF) mass spectrometry. Anal. Chem. *91*, 14552–14560. https://doi.org/10.1021/acs.analchem.9b03612.

Spraggins, J.M., Rizzo, D.G., Moore, J.L., Rose, K.L., Hammer, N.D., Skaar, E.P., and Caprioli, R.M. (2015). MALDI FTICR IMS of intact proteins: using mass accuracy to link protein images with proteomics data. J. Am. Soc. Mass Spectrom. *26*, 974–985. https://doi.org/10.1007/s13361-015-1147-5.

Staubitz, P., Neumann, H., Schneider, T., Wiedemann, I., and Peschel, A. (2004). MprF-mediated biosynthesis of lysylphosphatidylglycerol, an important determinant in staphylococcal defensin resistance. FEMS Microbiol. Lett. *231*, 67–71. https://doi.org/10.1016/s0378-1097(03)00921-2.

Thuny, F., Grisoli, D., Collart, F., Habib, G., and Raoult, D. (2012). Management of infective endocarditis: challenges and perspectives. Lancet *379*, 965–975. https://doi.org/10.1016/s0140-6736(11)60755-1.

Van de Plas, R., Yang, J., Spraggins, J., and Caprioli, R.M. (2015). Image fusion of mass spectrometry and microscopy: a multimodality paradigm for molecular tissue mapping. Nat. Methods *12*, 366–372. https://doi.org/10.1038/nmeth.3296.

Wakeman, C.A., Moore, J.L., Noto, M.J., Zhang, Y., Singleton, M.D., Prentice, B.M., Gilston, B.A., Doster, R.S., Gaddy, J.A., Chazin, W.J., et al. (2016). The innate immune protein calprotectin promotes *Pseudomonas aeruginosa* and *Staphylococcus aureus* interaction. Nat. Commun. *7*, 11951. https://doi.org/10.1038/ncomms11951.

Yang, J., and Caprioli, R.M. (2011). Matrix sublimation/recrystallization for imaging proteins by mass spectrometry at high spatial resolution. Anal. Chem. *83*, 5728–5734. https://doi.org/10.1021/ac200998a.

Yao, D., Yu, F.-y., Qin, Z.-q., Chen, C., He, S.-s., Chen, Z.-q., Zhang, X.-q., and Wang, L.-x. (2010). Molecular characterization of *Staphylococcus aureus* isolates causing skin and soft tissue infections (SSTIs). BMC Infect. Dis. *10*, 133. https://doi.org/10.1186/1471-2334-10-133.

Zavalin, A., Yang, J., Hayden, K., Vestal, M., and Caprioli, R.M. (2015). Tissue protein imaging at 1 μm laser spot diameter for high spatial resolution and high imaging speed using transmission geometry MALDI TOF MS. Anal. Bioanal. Chem. *407*, 2337–2342. https://doi.org/10.1007/s00216-015-8532-6.

STAR★METHODS

KEY RESOURCES TABLE

REAGENT or RESOURCE	SOURCE	IDENTIFIER
Antibodies		
Bacterial and virus strains		
Staphylococcus aureus Newman P_{mntA}*rfp*	Cassat et al. (2018)	Newman P_{mntA}*rfp*
Staphylococcus aureus Newman	Clinical Isolate, Duthie and Lorenz (1952)	Newman
Staphylococcus aureus Δ*mprF*	Peschel et al. (2001)	*mprF*::*erm*
Biological samples		
Human Infective Endocarditis Vegetations	Cleveland Clinic	Protocol #16-1521
Chemicals, peptides, and recombinant proteins		
1,5-diaminonapthalene (DAN)	Sigma Aldrich	D21200-25G, CAS: 2243-62-1
2,5-dihydroxyacetophenone (DHA)	Sigma Aldrich	D107603-25G, CAS: 490-78-8
Deposited data		
Data are available at Figshare	Figshare	https://doi.org/10.6084/m9.figshare.12780077.v2
Experimental models: Organisms/strains		
Female BALB/c mice (6–8 week old)	The Jackson Laboratory	JAX: 000,651
Oligonucleotides		
Recombinant DNA		
Software and algorithms		
Data Driven Image Fusion	Van de Plas et al. (2015)	https://fusion.vueinnovations.com/
SCiLS Lab, version 2019b	Bruker Daltonics, Billerica, MA, USA	https://www.bruker.com/products/mass-spectrometry-and-separations/ms-software/scils/overview.html

RESOURCE AVAILABILITY

Lead contact

Further information and requests for resources and reagents should be directed to and will be fulfilled by Jeffrey M. Spraggins (jeff.spraggins@vanderbilt.edu).

Materials availability

This study did not generate new unique reagents.

Data code and availability

- All data have been deposited at Figshare and are publicly available as of the date of publication. DOIs are listed in the key resources table.
- This paper does not report original code.
- Any additional information required to reanalyze the data reported in this paper is available from the lead contact upon request.

EXPERIMENTAL MODEL AND SUBJECT DETAILS

Bacterial strains and growth conditions

Bacterial strains, primers, and plasmids used in this study are listed in Table 2. Bacteria were routinely cultured at 37°C in Difco Tryptic Soy Broth (TSB) or on Tryptic Soy Agar (TSA) with 10 μg/mL erythromycin or 10 μg/mL chloramphenicol antibiotics supplemented as needed. All growth in liquid medium occurred in an Innova 44 incubator shaking at 180 rpm, unless otherwise noted. Fifteen-milliliter round-bottom polypropylene tubes with aeration lids incubated at a 45° angle were used for all standard cultures of 5 mL. The *S. aureus* clinical isolate strain Newman served as the genetic background for all experiments (Duthie and Lorenz, 1952). The construction of *S. aureus* strain Newman p.P_{mntA}*rfp* has been previously described (Cassat et al., 2019). The strain inactivated for lysyl-PG production (*mprF*::*erm)* has been previously described (Peschel et al., 2001).

Murine model of systemic *S. aureus* infection

All animal experimental protocols were reviewed and approved by the Vanderbilt University Institutional Animal Care and Use Committee (IACUC) and are in compliance with institutional policies, NIH guidelines, the Animal Welfare Act, and American Veterinary Medical Association guidelines on euthanasia. *S. aureus* strains were streaked from freezer stocks onto TSA with antibiotics, as required, and grown for 24 h at 37°C. Isolated colonies were used to prepare overnight cultures in 5 mL TSB. For all experiments, 6–8 week old female BALB/cJ mice (Jackson Laboratory) were retro-orbitally infected with 1×10^7 CFU in 100 μL of sterile phosphate-buffered saline as previously described (Corbin et al., 2008). Following infection, mice were humanely euthanized on day 4, 7, or 10. The kidney, hearts and livers were removed and immediately frozen on a bed of dry ice. Tissues were stored at −80°C until further processing.

Infective endocarditis vegetations

Vegetations were collected from a single patient prospectively during open-heart surgery for infective endocarditis under an approved Cleveland Clinic Institutional Review Board protocol with verbal patient consent (Protocol #16-1521). Visible blood clots on vegetations were removed with forceps and residual blood was reduced by extensive rinsing in phosphate buffered saline. Vegetations analyzed using mass spectrometry were snap-frozen in liquid nitrogen and stored at −80°C.

METHOD DETAILS

Materials

Ammonium formate, hematoxylin, and eosin were purchased from Sigma Aldrich (St. Louis, MO, USA). 1,5-diaminonapthaline (DAN) and 2,5-dihydroxyacetophenone (DHA) were also purchased from Sigma Aldrich (St. Louis, MO, USA) then purified by recrystallization. Indium tin oxide (ITO) coated slides were purchased from Delta Technologies, Limited (Loveland, CO, USA). All solvents (methanol, ethanol, acetonitrile, acetic acid, chloroform, and xylenes) and optimal cutting temperature compound were purchased from Fisher Scientific (Kalamazoo, MI, USA).

Sample preparation

Fresh frozen tissues were serially sectioned at 10 μm using a Leica CM3050 s cryostat (Leica Biosystems, Buffalo Grove, IL, USA) and thaw-mounted on glass microscope slides (Fisher Scientific, Kalamazoo, MI, USA) or indium tin oxide (ITO)-coated glass slides (Delta Technologies, Loveland, CO, USA. Sections were stored at −80°C until thawed for analysis under vacuum for approximately 15 min. MALDI matrix for lipid analysis was applied by a robotic aerosol sprayer (TM Sprayer, HTX Technologies, Chapel Hill, NC, USA). Samples for the analysis of lipids were washed using ammonium formate buffer as reported previously then homogeneously coated with DAN using optimized conditions at a surface density of 3.6 $\mu g/mm^2$ (Angel et al., 2012). Samples for the analysis of intact proteins were washed of lipids and salts as previously reported then homogenously coated with DHA using optimized conditions at a surface density of 3.1 $\mu g/mm^2$ (Zavalin et al., 2015). Samples for protein analysis were then recrystallized as previously reported (Yang and Caprioli, 2011). Post-MALDI IMS, tissue sections were washed of matrix using methanol and stained with hematoxylin and eosin (Fisher Scientific, Kalamazoo, MI, USA). Bright-field images of stained sections were acquired using a Leica SCN-400 optical slide scanner (Leica Biosystems, Buffalo Grove, IL, USA) at 20X magnification.

Fluorescence microscopy image acquisition

Fluorescence microscopy images were acquired from tissue sections on ITO-coated slides before tissue washing or matrix application using a fluorescence microscope (Nikon Eclipse 90i, Nikon Instruments Inc., Melville, NY, USA) equipped with a motorized stage and a 10X objective. Resulting pixel resolutions were 0.92 μm/pixel. A TRITC (excitation = 528–553, emission = 590–650) specific epifluorescence filter was used to visualize the RFP reporter at an exposure time of 40 ms. DAPI (excitation = 340–380, emission = 435–485) and FITC (excitation = 465–495, emission = 515–555) specific epifluorescence filters were used to allow visualization of tissue morphology by autofluorescence at exposure times of 100 ms and 150 ms, respectively.

Molecular image acquisition

MALDI IMS of lipids was performed using a modified 9.4T Fourier transform-ion cyclotron resonance mass spectrometer (FT-ICR MS) (SolariX, Bruker Daltonics, Billerica, MA, USA) equipped with an Apollo II dual MALDI/ESI source and a dynamically harmonized ParaCell. The source region of this instrument is modified with a secondary Gaussian laser, resulting in incident spots sizes of ~10 μm. Molecular images of lipids were acquired at pixel spacings of 15 μm for murine tissue (~10 μm laser beam size, 500 laser shots) and 40 μm for human tissue (~30 μm laser beam size, 500 laser shots) in both the *x* and *y* directions. Data were collected from m/z 200 to 2,000 in negative ionization mode with a resolving power ($m/\Delta m$) of ~50,000 at m/z 500. The time domain file size was set to 512k (free induction decay: 0.28 s). The ion optics were tuned to maximize transmission at the defined m/z range including the funnel RF amplitude (250 V_{pp}), source octopole (5 MHz, 400 V_{pp}), collision cell (collision cell voltage: 2.0 V, cell: 2 MHz, 1200 V_{pp}), time-of-flight delay (0.9 ms), transfer optics (4 MHz, 325 V_{pp}), and quadrupole (Q1 mass: m/z 350). The source DC optics were tuned to maximize ion transmission and observed intensities (capillary exit −190 V, deflector plate: −200 V, plate offset: −100 V, funnel 1: −100 V, skimmer 1: −20 V) as well as the ICR cell parameters (transfer exit lens: 10 V, analyzer entrance: 10 V, side kick: 0 V, side kick offset: 6.0 V, front trap plate: −1.200 V, and back trap plate: −1.205 V). Ion detection was performed using a sweep excitation power of 22%.

MALDI MS/MS of fluorescent foci was performed using a 15T FT-ICR MS (SolariX, Bruker Daltonics, Billerica, MA, USA) equipped with an Apollo II dual MALDI/ESI source and a dynamically harmonized ParaCell. The MALDI source employs a Smartbeam II 2 kHz, frequency tripled Nd:YAG (355 nm) laser. A spectrum was acquired using ~5,000 laser shots, rastered across fluorescent bacterial foci when compared to a fluorescent micrograph. Data were collected from m/z 49 to 900 in negative ionization mode. An isolation window of 5 Da and collision induced dissociation (CID) voltage of 23 V was used for MALDI MS/MS experiments.

MALDI IMS of intact proteins was performed using a 15T FT-ICR MS (SolariX, Bruker Daltonics, Billerica, MA, USA) equipped with an Apollo II dual MALDI/ESI source and a dynamically harmonized ParaCell. The MALDI source employs a Smartbeam II 2 kHz, frequency tripled Nd:YAG (355 nm) laser. Molecular images of intact proteins were acquired at pixel spacings of 100 μm for murine tissue with a ~50 μm laser beam size (750 laser shots) in both the *x* and *y* directions. Data were collected from m/z 2,000 to 30,000 in positive ionization mode with a resolving power ($m/\Delta m$) of ~60,000 at m/z 10,000. The time domain file size was set to 1M (free induction decay: 4.61 s). The ion optics were tuned to maximize transmission at the defined m/z range including the funnel RF amplitude (285 V_{pp}), source octopole (2 MHz, 525 V_{pp}), collision cell (collision cell voltage: −8.0 V, cell: 1.4 MHz, 1850 V_{pp}), time-of-flight delay (3.00 ms), transfer optics (1 MHz, 410 V_{pp}), and quadrupole (Q1 mass: m/z 1,000). The source DC optics were tuned to maximize ion transmission and observed intensities (capillary exit 250 V, deflector plate: 200 V, plate offset: 100 V, funnel 1: 150 V, skimmer 1: 60 V) as well as the ICR cell parameters (transfer exit lens: −20 V, analyzer entrance: −10 V, side kick: 0 V, side kick offset: −1.5 V, shimming DC bias: 1.5 V, and gated injection DC bias: 1.5 V, back trap plate quench: −30 V). The gated trapping and detection function of the ICR cell was enabled (front and back plates for trapping: 2.5 V, front and back plates for detection: 1.1 V, ramp time: 0.01 s). Ion detection was performed using a sweep excitation power of 45%. FlexImaging 5.0 (Bruker Daltonics, Billerica, MA, USA) and SCiLS Lab (version 2016b, Bruker Daltonics, Billerica, MA, USA) were used to normalize intensities (root mean squared) and visualize ion images.

Protein extraction for LC-MS/MS

Methods for LC-MS/MS analysis were previously published with extensive details (Martin et al., 2020). Approximately 150-200 mg of each vegetation was homogenized in 1 mL of T-Per (ThermoFisher Scientific, Waltham, MA, USA) extraction buffer supplemented with protease inhibitor (cOmplete tablets, Roche, Millipore Sigma, Burlington, MA, USA) using a T10 ultra Turrax (IKA, Staufen, Germany) homogenizer, boiled at 95°C for 5 min and cooled to room temperature before adding 1 μL of benzonase (Millipore Sigma, Burlington, MA, USA). The homogenates were tip-probe sonicated at 20% amperage with 3 sec on/off intervals a total of six times using a Q-500 sonicator (Qsonica, Newtown, CT, USA), centrifuged at 15,000 *xg* for 10 min, and the supernatant was retained for analysis as the soluble fraction (T-Per fraction). The pellet was washed twice with cold PBS and resuspended in a chaotropic buffer (5 M GuHCL, 1% CHAPS, 25 mM $NAC_2H_3O_2$, 50 mM aminocaproic acid, 5 mM NA_2EDTA) supplemented with protease inhibitor (cOmplete tablets, Roche, Millipore Sigma, Burlington, MA, USA) at 4°C with rotation for 72 h, centrifuged at 17,000 *xg* for 10 min and the supernatant was retained for analysis as the matrix fraction. Fractions were analyzed separately, and data were combined by sample post database search analysis.

LC-MS/MS proteomics data acquisition and analysis

Peptide samples were analyzed using a ThermoFisher Scientific Fusion Lumos tribrid mass spectrometer system interfaced with a Thermo Ultimate 3000 UHPLC. The HPLC column was a Dionex 15 cm × 75 μm id Acclaim Pepmap C18, 2 μm, 100 Å reversed phase capillary chromatography column. Five μL volumes of the trypsin-digested extract were injected, peptides were eluted from the column by an acetonitrile/0.1% formic acid gradient at a flow rate of 0.3 μL/min and introduced in-line into the mass spectrometer over a 120 min gradient. The nanospray ion source was operated at 1.9 kV. The digest was analyzed using a data-dependent method with 35% collision-induced dissociation fragmentation of the most abundant peptides every 3 s and an isolation window of 0.7 m/z. Scans were conducted at a maximum resolution of 120,000 at m/z 200 for full MS and 60,000 at m/z 200 for MS/MS. Individual LC-MS/MS raw files were searched against a human database (Uniprot.org) using Proteome Discoverer 2.2 (ThermoFisher Scientific, Waltham, MA, USA). Peptides were identified using a precursor mass tolerance of 10 ppm, and fragment mass tolerance of 0.6 Da. The only static modification was carbamidomethyl (C), whereas dynamic modifications included the light (28.03 Da) dimethyl formaldehyde (N-terminal, K), oxidation (M), deamidation (N, R (citrullination)), acetylation (N-terminal), and Gln to pyro-Glu N-terminal cyclization. Peptides were validated using a false discovery rate (FDR) of 1% against a decoy database. Only high confidence proteins (containing peptides at a 99% confidence level or higher) were recorded from each sample for data analysis. When a peptide corresponding to multiple proteins was identified, all protein accession numbers were reported. However, when labeled as protein groups, peptides corresponding to multiple accession numbers were assigned to one master protein accession (based the number of unique peptides in each accession and overall sequence length of the protein, e.g., ACTG2, ACTB, ACTA1, and ACTA2 have peptides with same sequence, but only the protein which has a unique peptide(s) found is considered a master protein, and all others are combined into the same protein group).

LC-MS/MS of lipids from *S. aureus* culture

LC-MS/MS of lipids from *S. aureus* culture was completed to relate identifications to ions within IMS data. Separations and analyses were adapted from previously published methods (Laut et al., 2020). Lipids were extracted from cell pellets (normalized by OD_{600}) using the Bligh-Dyer method (Bligh and Dyer, 1959). Extracts were dried under nitrogen and reconstituted in 100 μL of 65% acetonitrile, 30% isopropyl alcohol, and 5% water. A 15 μL volume of each sample was injected into an Acquity Arc ultra-high-performance

liquid chromatography (UPLC) system (Waters Corporation, Milford, MA, USA). Lipids were separated using an Acquity UPLC HSS C18 column (Waters Corporation, Milford, MA, USA) with 1.8 μm particle size and dimensions of 2.1 mm by 150 mm. The aqueous solvent system (solvent A) consisted of 60% acetonitrile, 40% water, 0.1% formic acid, and 10 mM ammonium acetate. The organic solvent system (solvent B) consisted of 90% isopropyl alcohol, 10% acetonitrile, 10 mM ammonium acetate, and 0.1% formic acid (100). The following gradient was used: 0 min, 70% solvent A; 0 to 5 min, 70%–57% solvent A; 5 to 5.1 min, 57%–50% solvent A; 5.1 to 14 min, 50%–30% solvent A; 14 to 21 min, 30%–1% solvent A; 21 to 30 min, 1% solvent A; 30 to 30.1 min, 1%–70% A. The column was allowed to equilibrate at 70% solvent A for 9.9 min prior to the next injection. The column heater was set at 40°C, and the flow rate was 0.22 mL/min. After separation, samples were introduced by electrospray ionization (2.5-kV capillary; 100°C source temperature; 40-V sampling cone) into a quadrupole-time of flight mass spectrometer (Waters Synapt G2-Si; Waters Corporation, Milford, MA, USA) for analysis in negative-ionization mode (trap and transfer collision energies, 15 V; resolution mode; ion mobility not enabled). Samples were analyzed in data-dependent mode with a survey window at mass-to-charge (m/z) ratios of 500 to 1,750 with a scan time of 0.2 s. Fragmentation data were acquired using a collision energy ramp of 6–147 eV (depending on the m/z value selected) with a 30-s exclusion window. The instrument was calibrated using sodium formate prior to analysis. PG and lysyl-PG lipids eluted between 17 and 24 min.

QUANTIFICATION AND STATISTICAL ANALYSIS

Biological (2) replicates of IMS experiments were completed for the *S. aureus* murine infection model to ensure reproducibility. Experiments were only completed twice due to large data sizes and lengthy analysis times. Ion intensity noise in MALDI IMS experiments was addressed using root mean squared (RMS) intensity normalization.

Data-driven image fusion

For image fusion analysis with IMS data sets, the mass spectrometry data were treated as a data cube in which the x and y coordinates are pixel dimensions and the z coordinate is m/z. Analogously, the microscopy data map pixel dimensions are x and y, but the z coordinate was the color channels. Image fusion algorithms were used to train a cross-modality model. The model was subsequently opened up to retrieve relative slope coefficients as heuristics for correlations between the microscopy and IMS channels, effectively highlighting image pairs of IMS and fluorescence micrograph data that seem to exhibit potential relationships. In the present work, relationships were mined to identify ions of interest that relate to the red color channel, to discover correlations between IMS-reported ions and the bacterial RFP fluorophore reporter after image registration (Figure S2). Further information on this algorithm can be found in previous work (Van de Plas et al., 2015).